1 The role of lithospheric thermal structure in the development of
2 lateral heterogeneous of the continental collision system

3 Mengxue Liu[1], Dinghui Yang[1], Rui Qi[1]

4 [1]Department of Mathematical Sciences, Tsinghua University, Beijing 100084, China.

5 *Correspondence to*: Dinghui Yang (ydh@mail.tsinghua.edu.cn)

6 **Abstract.** Continental collision is a crucial process in plate tectonics, whereas our understanding regarding the tectonic

7 complexities at such convergent plate boundary remains largely unclear in terms of the evolution and the controlling

8 parameters of its lateral heterogeneity. In this study, we conducted a series of two-dimensional numerical experiments to

9 investigate how continental lithospheric thermal structure influences the development of lateral heterogeneity along the

10 continental collision zone. Two end members were achieved: 1) Continuous subduction mode, which prevails when the

11 model has a cold procontinental moho (Tmoho $\leq$ 450 °C). In this case, a narrow collision orogen develops, and the

12 subducting angle steepens with the increasing retrocontinental Tmoho. 2) Continental subduction with a slab break-off,

13 which generates a relative wide collision orogen, and dominates when the model has a relative hot procontinental Tmoho ($\geq$

14 500 °C), especially when the Tmoho $\geq$ 550°C. In contrast, Hr is the second-order controlling parameter in varying the

15 continental collision mode, while it prefers to enhance strain localization in the upper part of the continental lithosphere and

16 promote the growth of shear zones there. By comparing the model results with geoscience observations, we suggest that the

17 discrepant evolutionary paths from the continuous subduction underlying the Hindu Kush to the continental subduction after

18 slab break-off beneath eastern Tibet may originate from the inherited lateral inhomogeneity of Indian lithospheric thermal

19 structure. Besides, the high content of crustal radioactive elements may be one of the important factors that controls the

20 formation of large thrust fault zones in the Himalayas.

21 1 Introduction

22 Continental collision following the closure of the ocean is regarded as one of the key geodynamical processes of plate

23 tectonics (Toussaint et al., 2004), which creates the world's largest orogen (the Alpine-Himalaya orogen) and highest plateau

24 (the Tibetan Plateau). It would be really hard to maintain a homogeneous plate morphology and the crustal-mantle

25 deformation features during such a large-scale collision stretching thousands of kilometers. Many of the previous geoscience

26 observations have already provided insights into the significant lateral heterogeneity of Himalayan-Tibetan orogen (Zhou

27 and Murphy, 2005; Li et al., 2008; Chen et al., 2015). Specifically, the horizontal sliding distance and subducting angle of

28 the Indian lithosphere vary laterally from west to east. Despite various mechanisms have been invoked, including

29 inhomogeneous inherit lithospheric structure, variations in rock composition, characters of terrane assembly, and the

30 complex tectonic settings (Chen et al., 2016; Vogt et al., 2018; Liu and Yang, 2022), the development of the collision zone's

31 lateral heterogeneity remains ambiguous and requires further investigations.

32 Many of the laboratory experiments (Willingshofer and Sokoutis, 2009; Luth et al., 2010) and numerical modeling

33 (Beaumont et al., 1994; Pysklywec, 2001; Toussaint et al., 2004; Huangfu et al., 2017; Liao and Gerya, 2017; Vogt et al.,

34 2018; Liu et al., 2022b) have manifested that lithospheric thermal structure is one of the important controlling parameters

35 contributing to the regulation the evolution of continental collision (Pysklywec, 2001; Faccenda et al., 2008; Ueda et al.,

36 2012; Tang et al., 2020; Liu et al., 2022a). Pysklywec (2001) once used a series of thermomechanical models that focused on

37 the evolutionary modes of the continental lithospheric mantle during collision. The experiments suggested that an increase in

38 lithospheric geotherm resulted in a transition of the lithospheric mantle from an asymmetric, subduction-like mode to

39 ablative subduction. Similarly, on the basis of two-dimensional mechanical models, Toussaint et al. (2004) investigated the

40 potential scenarios for the evolution of continental collision. They concluded that models with a relatively low (< 550 ˚C)

41 moho temperature and a fast convergent rate (> 5 cm/yr) are more likely to maintain stable subduction. On the contrary,

42 among warmer and slower convergent models, lithospheric folding, pure-shear thickening, and Rayleigh-Taylor (RT)

43 instabilities prevailed. Ghazian and Buiter (2013) used 2D numerical models to discuss the sensitivity of various collision

44 modes to velocity, crust-mantle temperature structure, lithospheric rheology, and the density difference between the

45 lithospheric mantle and asthenosphere. They recognized that velocity, lithospheric rheology, and temperature have important

46 controls. More precisely, stable continental subduction evolves over a large range of values for convergent velocity and

47 lithospheric temperature. Fast and cold models tend to fold, while slow and warm ones can generate RT-type dripping.

48 Heron and Pysklywec (2016) subsequently presented dynamic thermomechanical experiments to explore the role of

49 lithospheric inherited weakness in the orogenic process. According to their model results, lithospheric temperature exerts a

50 strong control on lithospheric strength; it may influence the brittle-ductile transition depth to help determine which layer

51 (upper crust, lower crust, or lithospheric mantle) dominantly controls the lithospheric deformation style in a collision system.

52 Recently, Huangfu et al. (2019) employed systematic numerical simulations to study the dynamics of the lithospheric-scale

53 subduction and crustal-scale underthrusting of the continental collision zone. They found that models with low convergence

54 velocity and a cold upper plate are inclined to lithospheric-scale subduction, whereas models with high velocity and a hot

55 overriding plate contribute to crustal-scale underthrusting. Though numerous numerical simulations are employed to qualify

56 the effects of lithospheric thermal structure, it is noteworthy, however, that earlier studies consistently mainly focused on the

57 influences of the overriding lithospheric thermal structure. Otherwise, a fairly large number of them neglected oceanic

58 subduction prior to the continental collision for simplicity. Thus, our understanding of tectonic complexities that may emerge

59 during progressive crust-mantle deformation at the convergent plate boundary remains largely unclear.

60 Here we present a series of high-resolution numerical experiments to gain new insights on how continental

61 lithospheric thermal structure varies the evolutionary path of the continental collision system. Temperature heterogeneities

62 are incorporated by altering the continental moho temperature (Tmoho) and crustal radioactive heat production (Hr),

63 respectively (See Table S2 in Supporting Information for the model list). In the end, our model results are applied to draw

64 some parallels with the Indian-Asian collision zone.

2 Materials and Methods

2.1 Governing equation

67   We use the parallel code **A**dvanced **S**olver for **P**roblems in **E**arth's **C**onvec**T**ion (ASPECT) (Kronbichler et al., 2012),

68 an extensible code of the C++ program library deal.ii (**D**ifferential **E**quations **A**nalysis **L**ibrary, https://www.dealii.org/),

69 targeted at the computational solution of partial differential equations using adaptive finite elements (Arndt et al., 2021), to

70 solve three conservation equations. The methodology is similar to our recent work (Liu and Yang, 2022; Liu et al., 2022a),

71 and we quoted directly from these publications. The models are calculated by solving the following equations of

72 conservation of mass, momentum, and internal energy for an incompressible medium and adopting the extended Boussinesq

73 approximation (van Zelst, 2022).

74
$$-\nabla \cdot 2\eta \dot{\varepsilon}(\boldsymbol{u}) + \nabla p = \rho \mathbf{g} \qquad \text{in } \Omega, \tag{1}$$

75
$$\nabla \cdot \boldsymbol{u} = 0 \qquad \text{in } \Omega, \tag{2}$$

76
$$\rho_0 C_p \left(\frac{\partial T}{\partial t} + \boldsymbol{u} \cdot \nabla T \right) - \nabla \cdot k \nabla T = \rho_0 H \tag{3}$$

77
$$+ 2\eta \, \dot{\varepsilon}(\boldsymbol{u}) : \dot{\varepsilon}(\boldsymbol{u})$$

78
$$+ \alpha T (\boldsymbol{u} \cdot \nabla P) \qquad \text{in } \Omega$$

79
$$\frac{\partial c_i}{\partial t} + \boldsymbol{u} \cdot \nabla c_i = 0 \tag{4}$$

80 On the right hand-side of Eq. (3), the three terms represent the internal heat production that includes radioactive decay,

81 friction heating, and adiabatic compression of material. η is the viscosity, $\dot{\varepsilon}(\boldsymbol{u}) = \frac{1}{2}(\nabla \boldsymbol{u} + \nabla \boldsymbol{u}^{\mathrm{T}})$ is the deviator of the strain

82 rate tensor, $\boldsymbol{u}$ is the velocity, p is the pressure, $\mathbf{g}$ is the gravitational acceleration, Ω is the interesting domain, C_p is the heat

83 capacity, k is the heat conductivity, H is the intrinsic specific heat production, α is the thermal expansion coefficient, ρ_0 is

84 the adiabatic reference density. c_i named compositional fields here (e.g., upper crust, lower crust, Kronbichler et al., 2012).

85 As the medium was considered incompressible, we assumed that the density (ρ) in Eq. (1) satisfied the equation:

86
$$\rho = \rho_0 \left(1 - \alpha (T - T_0) \right) \tag{5}$$

87 where ρ_0 is the reference density at reference temperature T_0 (293 K).

2.2 Rheology

89   Our models are based on the common assumption that solid earth materials are treated as highly viscous fluids. Thus,
90   we apply a viscoplastic rheology (Glerum et al., 2018). The viscous regime uses a composite of diffusion and dislocation
91   creep that can be conveniently formulated as follows: (Karato and Wu, 1993; Karato, 2008).

92
$$\eta_{\text{diff/disl}} = \frac{1}{2} A_{diff/disl}^{-\frac{1}{n}} \mathrm{d}^{\frac{m}{n}} \dot{\varepsilon}_e^{\frac{1-n}{n}} \exp\left(\frac{Q_{diff/disl}+PV_{diss/disl}}{nRT}\right) \tag{6}$$

93
$$\eta_{\text{comp}} = \left(\frac{1}{\eta_{\text{diff}}} + \frac{1}{\eta_{\text{disl}}}\right)^{-1} \tag{7}$$

94   where $\dot{\varepsilon}_e$ is the square root of second invariant of the deviatoric strain rate. In the case of diffusion creep, $n = 1$, m > 0, while
95   for dislocation creep $n > 1$, m = 0. Definitions and values of other symbols are shown in Table S1 in Supporting Information.
96   Surface erosion and sedimentation are neglected.

97   The plastic yielding is defined by the Drucker–Prager criterion as Eq. (8) (Davis and Selvadurai, 2002):

98
$$\eta_{\text{yield}} = \frac{C \cos(\phi) + P \sin(\phi)}{2\dot{\varepsilon}_e} \tag{8}$$

99   Where C is the cohesion and ϕ is the initial friction angle. We also include strain weakening in the plastic regime, through
100   which C and ϕ are linearly weakened by a factor of 2 or 4 between plastic strains of 0.5 and 1.5.
101   The effective viscosity is eventually given by:

102
$$\eta_{\text{eff}} = \min\left(\max\left(\eta_{\text{i}}, \eta_{\text{min}}\right), \eta_{\text{max}}\right) \tag{9}$$

103   where i is one of the subscripts among diff, disl, comp, and yield. η_{max} and η_{min} are user-defined viscosity cutoffs.

2.3 Initial model configuration and boundary conditions

105   The numerical model domain is 2000 km × 660 km in the horizontal and vertical directions. It contains a
106   retrocontinental lithosphere and a procontinental lithosphere, with an oceanic lithosphere in between (Fig. 1). The
107   continental lithosphere is 120 km thick, consists of a 25-km-thick upper crust (wet quartzite, Gleason and Tullis, 1995), a 10-
108   km lower crust (wet anorthite, Rybacki et al., 2006), and an 85-km lithospheric mantle. The oceanic lithosphere contains a 4-
109   km-thick sediment layer (gabbro, Wilks and Carter, 1990), an 8-km-thick oceanic crust layer (gabbro, Wilks and Carter,
110   1990), and an 88-km-thick lithospheric mantle. Dry olivine (Hirth and Kohlstedt, 2003) is used for the mantle. All material
111   properties are listed in Table S1. The numerical resolution incrementally increases along the depth direction from 2 km to 8
112   km.

113   Temperature is fixed at the model surface (0˚C) and the base of the lithosphere (1300˚C), while various continental
114   T_{moho} is defined ranging from 450 – 600 ˚C. The initial continental lithospheric temperature profile follows Chapman (1986),
115   taking into account the thickness of each lithologic layer (Eqs. (11) - (13)). The oceanic lithospheric temperature distribution

116 follows the plate cooling model (Turcotte and Schubert, 2002). Besides, a temperature gradient of 0.5 ˚C/km is assumed for
117 the sublithospheric mantle.

$$T_Z = T_T - \frac{q_T}{k} Z - \frac{H\,Z^2}{2k} \tag{11}$$

$$T_B = T_T + \frac{q_T}{k}\Delta Z - \frac{H\,\Delta Z^2}{2k} \tag{12}$$

$$q_B = q_T - H\Delta Z \tag{13}$$

121 T_Z is the temperature at depth Z; T is the temperature, q is the heat flux, the subscript T and B denote the top and
122 bottom boundaries of each lithologic layer, respectively; ΔZ is the layer thickness; H is the volumetric heat production; k is
123 the thermal conductivity.

124 We apply a free surface and free slip lower boundary, and impose a 5 cm/yr convergence rate to the trailing end of the
125 procontinental lithosphere. Equivalent material flows out through both side walls of the mantle domain to keep mass balance
126 within the whole computational domain (Fig. 1).

127
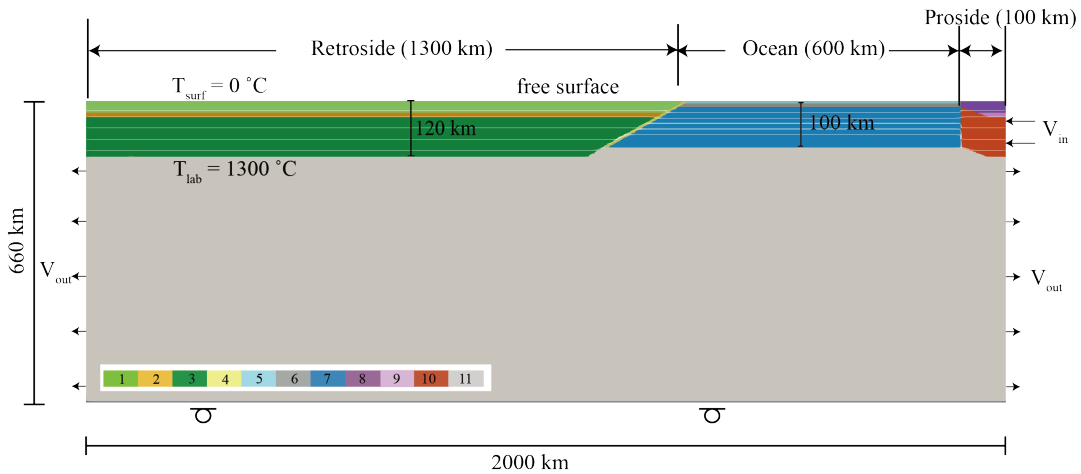
Figure 1. Reference model configuration and boundary conditions. Different colors reflect different lithologies: 1, 8,
continental upper crust; 2, 9, continental lower crust; 3, 10, continental lithospheric mantle; 4, weak zone; 5, sediment; 6,
oceanic crust; 7, oceanic lithospheric mantle; 11, sub-lithospheric mantle (Table S1). The white lines are isotherms of 200 ˚C
increments in the range of 200 ˚C to 1200 ˚C. T_{surf} is the surface temperature, T_{lab} is the bottom temperature of continental
lithosphere. V_{in} and V_{out} denote where material flows in and out.

3 Results

134 We conducted 48 numerical experiments by varying continental T_{moho} and crustal H_r to mimic different continental
135 thermal structures. Two distinct continental collision evolutionary paths were recognized: (I) continuous subduction and (II)
136 continental subduction with a slab break-off. All the simulations are summarized in Table S2.

3.1 Continuous subduction without slab break-off (Mode I)

Figure 2 shows the development of the continuous subduction mode, it takes the Model m2 (reference model, Table S2) as an example. The model started with a relative shallow angle subduction characterized by the oceanic plate dips downward along the low-viscosity weak zone (Fig. 2a1, 3 Myr). During this stage, a portion of oceanic sediment was scraped off and stacked at shallow, accompanied by the slight uplift of the retrocontinental foreland (Fig. 2a2, 2c). As the subduction goes on, the dipping angle of the slab in depth gradually steepens under the increasing slab pull (Fig. 2a2, 9 Myr). At ~11.5 Myr (Fig. 2a3), continents collide with each other after the fully consumption of the oceanic plate. Under the continued oceanic slab pulling, the procontinental lithosphere inherited the subduction, characterized by further subducting angle steepening that resulted in the superposition of retrocontinental upper crust and oceanic sediment on the procontinental forepart. With the proceeding of procontinental subduction, the collision wedge uplifted prominently (Fig. 2c). After that, a large part of the oceanic sediment previously preserved at shallow was then entrained and subducted with the procontinental crust, followed by the rapid uplift at the retroside of the collision zone and the retroward advance of suture (Fig. 2c). From ~17.5 Myr on, the buoyant procontinental upper crust initiated to detach from the underlying lithosphere, mixed with the exhumated oceanic sediment, accumulated together in the subduction channel, and broke the neighboring retrolithopheric mantle (Figs. 2a4, 2a5). During this time, uplift within the collision zone gradually expands to the retrocontinental interior (Fig. 2c).
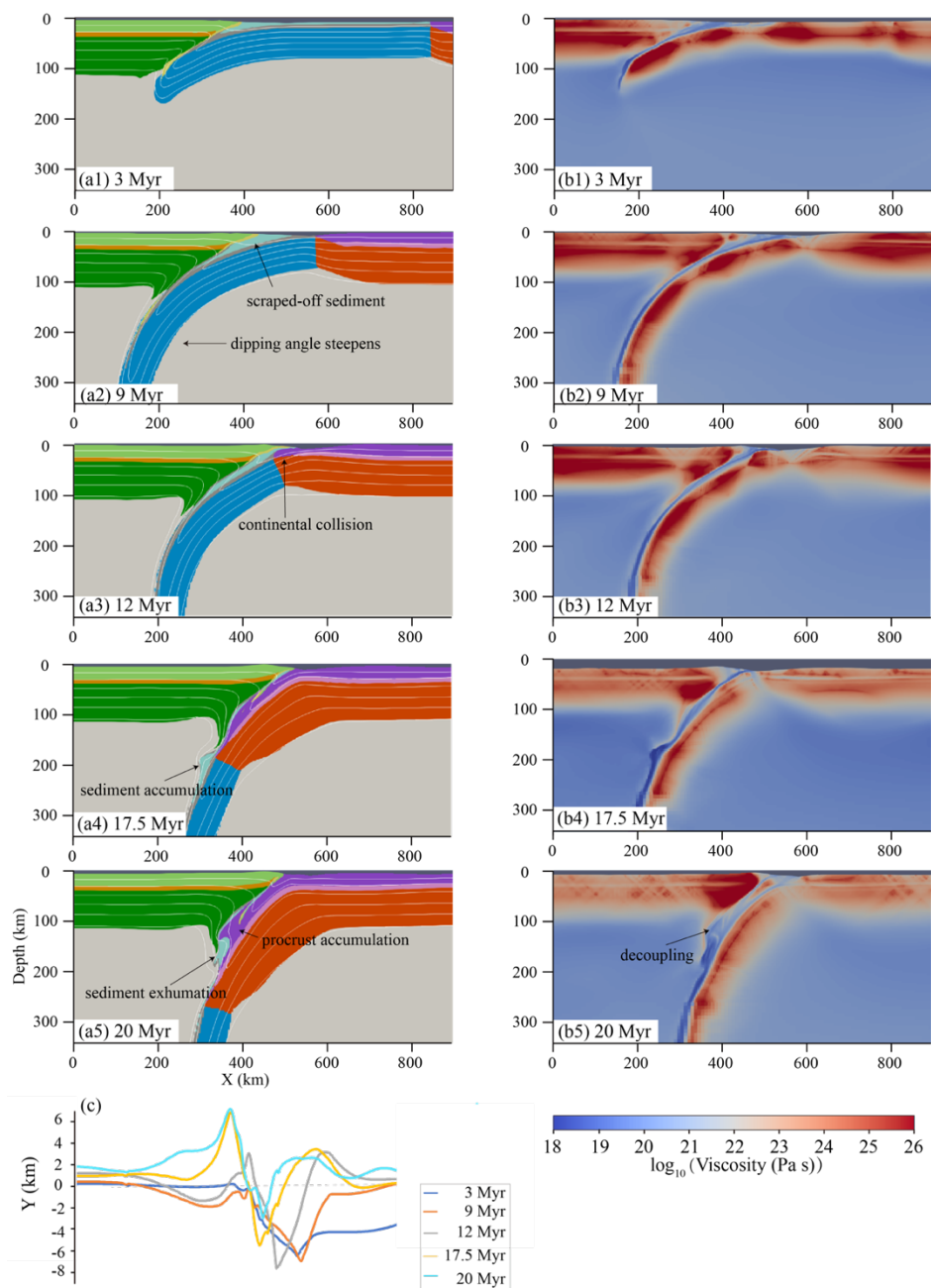
Figure 2. Time evolution of Model m2. Snapshots of compositional fields (a1 - a5), viscosity (b1 - b5) and topography (c) for selected model times are shown. The lithologies and isotherms are the same as in Fig. 1.3 Sensitivity 3.2 Continental subduction with a slab break-off (Mode II)

3.2 Continental subduction with a slab break-off (Mode II)

In Model m7, both the pro- and retro- continent have higher T_{moho} than Model m2 (Table S2). The lithospheric deformation behaviors and the evolution of the model during the oceanic subduction phase are quite similar to those observed in Model m2 (Fig. 3a1). The only difference is that the slab steepened more rapidly at a later stage, which gave rise to the decoupling between the retrocontinental lithosphere and the oceanic plate. Such a process created an ideal space for the asthenospheric upwelling and resulted in the significant weakening of the retrocontinental lithosphere (Fig. 3a2, 8.5 Myr). After ~10.2 Myr, combined effect of the increasing slab pull and asthenosphere upwelling promoted necking around the oceanic-procontinental lithospheric transition zone (Fig. 3a3, 11 Myr). The procontinental lithosphere then arrived at the trench and initiated subducting along the inclined weak zone, accommodating most of the ongoing convergence. During this stage, the continuous compression and rebound after slab break-off significantly uplifted the collision zone. Later on, the upper part of the retrocontinental lithosphere indented into the procrust, scraping off most of the procontinental upper crust, causing significant thickening and localized shear zones there while leaving the residual little portion to subduct with the lithosphere. Subsequently, the accumulated orogenic wedge gradually grew into a relative wide surface uplift.
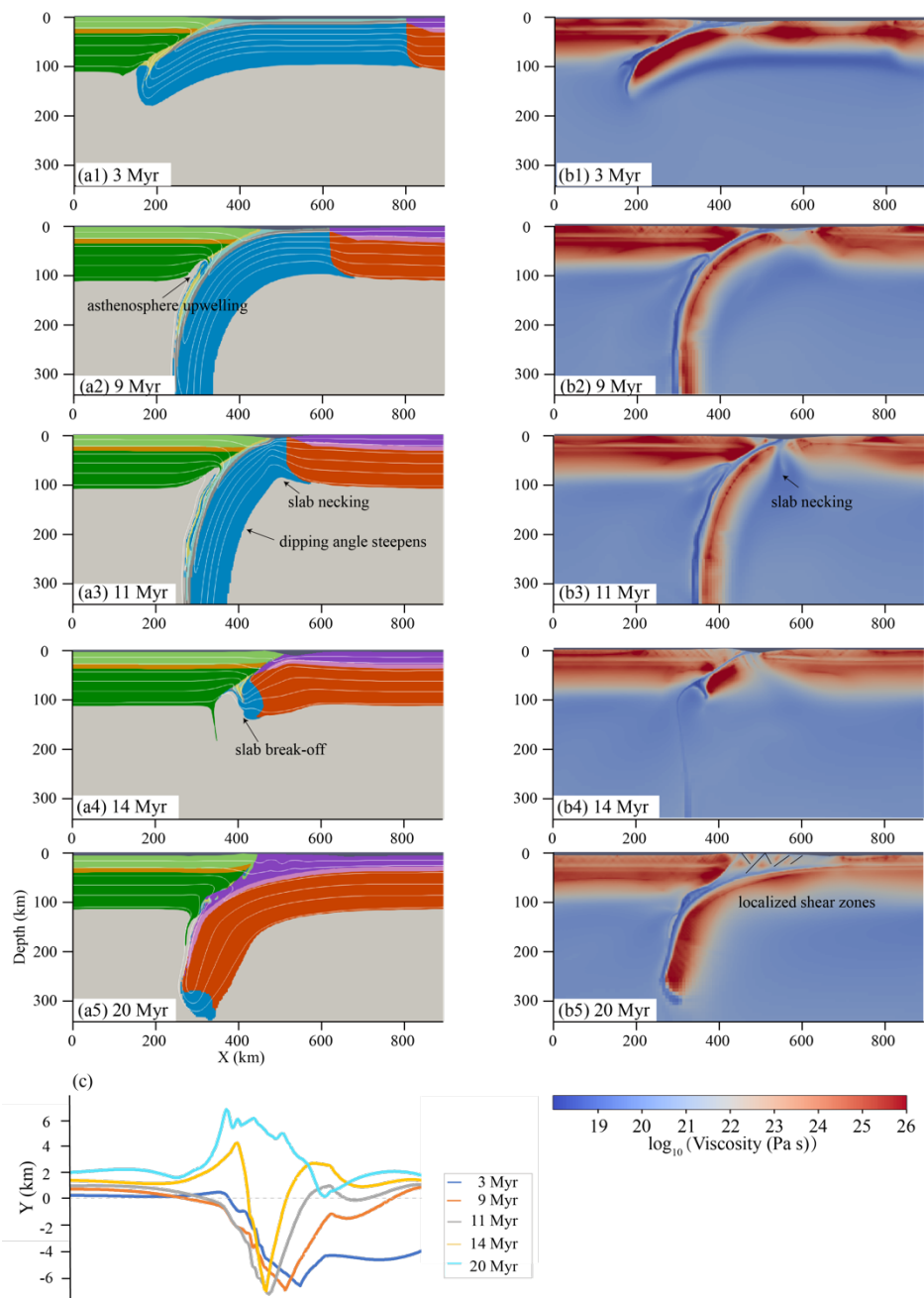
Figure 3. Results of Model m7. Snapshots of compositional fields (a1 - a5), viscosity (b1 - b5) and topography (c) for selected model times are shown. The lithologies and isotherms are the same as in Fig. 1.

3.3 Sensitivity tests of lithospheric thermal structure on the evolution of continental convergence

A regime diagram (Fig. 4) of all the models summarizes the template simulations investigating the effects of continental T_{moho} and H_r, and two contrasting end members of continental collision modes are identified. Models with a cold procontinental T_{moho} (≤ 450 °C) generally exhibit a continuous subduction mode without slab break-off. Meanwhile, the hotter the retrocontinental T_{moho}, the steeper the subducting angle is (Figs. 4a, 5a). In comparison, Mode II dominates among the models with a relative hot procontinental T_{moho} (≥ 500 °C), especially when the retrocontinental T_{moho} is greater than 550°C (Fig. 4a). In addition, H_r is a second-order controlling parameter compared to the T_{moho}, as it's more propensity to alter the upper part of lithospheric deformation styles than the continental collision mode (Figs. 6c - 6i).
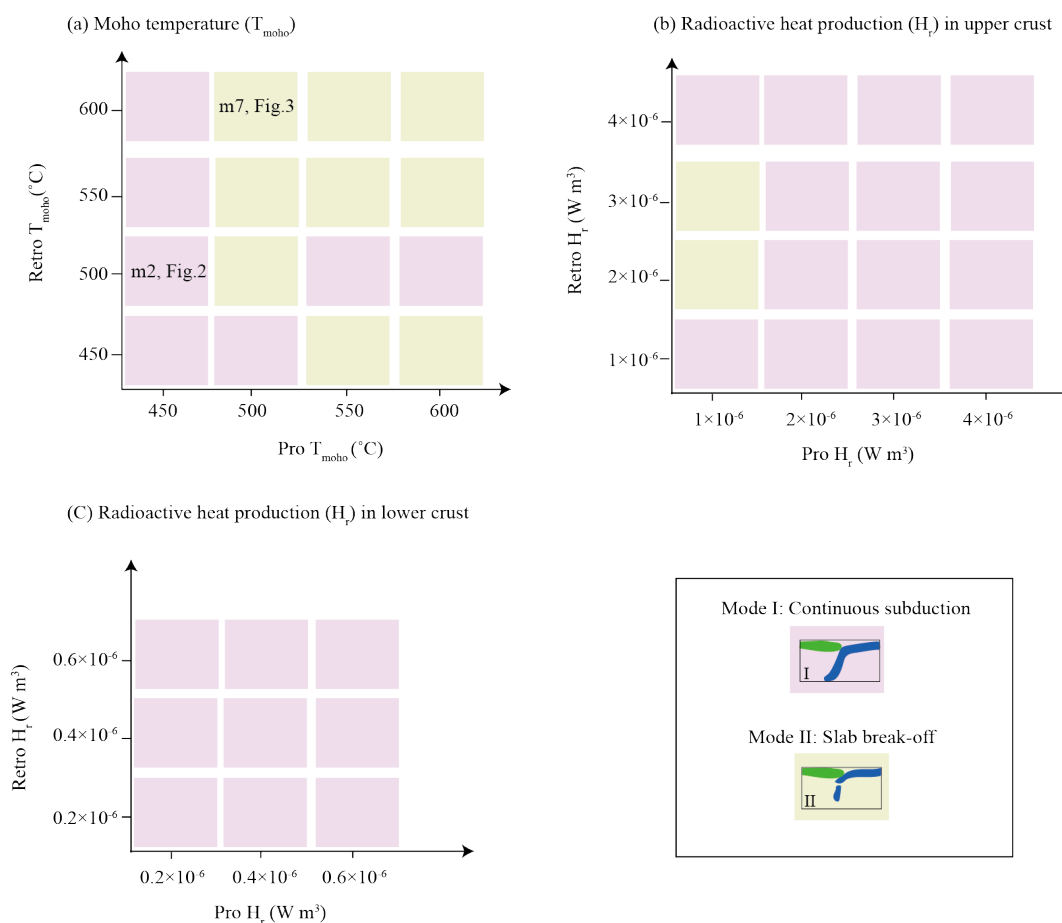
Figure 4. Schematic figures of models with different (a) continental T_{moho}, (b) upper and (c) lower crustal radioactive heat production (Table S2). The diagram in each panel shows the dependence of collision mode on the corresponding controlling parameters of both colliding plates.

4 Discussions

4.1 How continental moho temperature influences the trajectory of the collision system?

As mentioned above, models incorporating a cold prolithosphere generally evolve into continuous subduction without slab break-off. It may come from the fact that a cold prolithosphere is strong enough to maintain its strength, and also keeps coupling with the retrolithophere during plate convergence. Thus, the prolithosphere suffers moderate roll-back, under the condition that the stress is not sufficient to yield the lithosphere and generate break-off (Fig. 2, Fig. S1 in Supporting Information). Based on further analysis of this mode of models, we notice that the subducting angle increases as the retrocontinental T_{moho} increases, accompanied by much more procrust accumulation at shallow and intense retrolithospheric mantle destruction (Figs. 5a - 5d). The mechanism behind this is that increasing the retrocontinental T_{moho} can weaken the retrolithosphere and increase the thermal structural difference between the two continents, which may lead to plate decoupling. As a consequence, it is more likely for the prolithosphere to roll back as the magnitude of decoupling increases. Besides, weakening of the retrolithosphere may also offer a favorable condition for the intrusion of accumulated procrustal material into it.

As to mode II, models with hot procontinental T_{moho} ($\geq 500°C$) always evolve into continental subduction following a slab break-off. In these cases, when the retrocontinental T_{moho} is defined, the time for the slab break-off increases as the procontinental T_{moho} decreases (Fig. 5e). We perceive that the plates decoupling also enhances when retro T_{moho} increases, as shown in mode I. The hotter the procontinent, the weaker and easier it is to break. As a result of ongoing subduction, the slab rolls back rapidly, which may generate a gap between the adjacent plates. The asthenosphere then upwells into it, and in turn aggravates the roll-back. This contributes to the development of intense strain localization in the prolithosphere and finally leads to slab break-off (Figs. 3, S2, 5f, 5g, 5h).

206
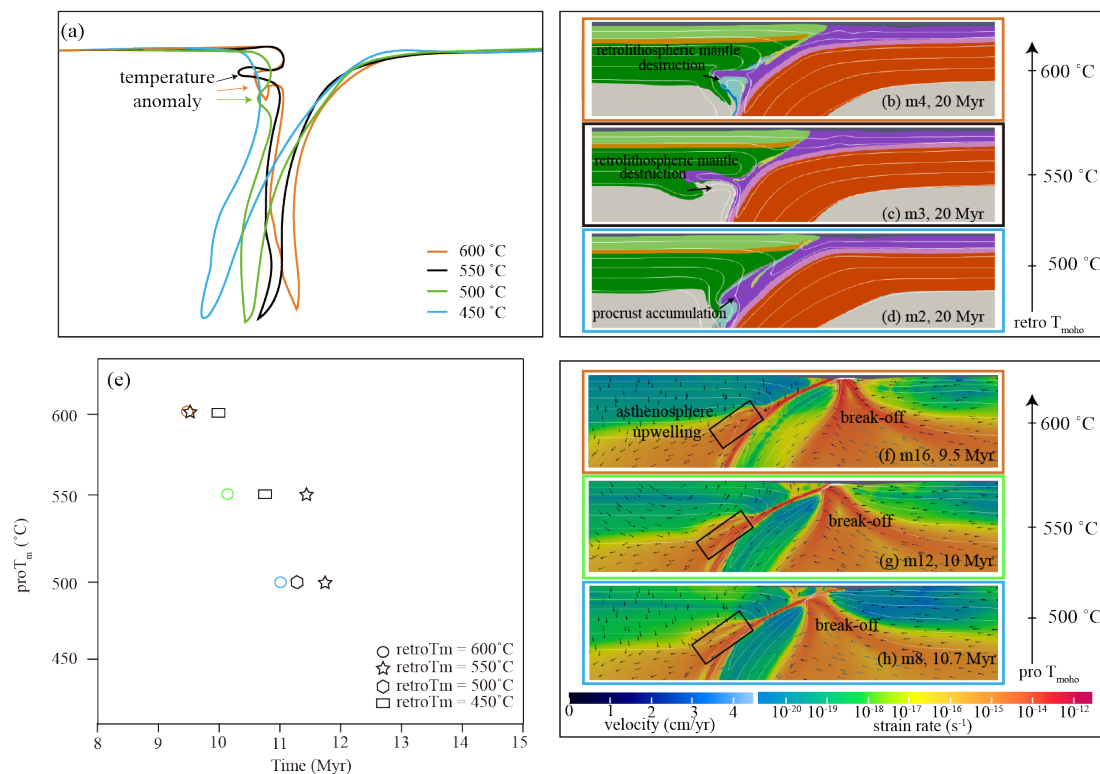
Figure 5. (a) Geometries of subducting plate in models with different retrocontinental T_{moho}. Compositional fields of models with decreasing retrocontinental T_{moho}, (b) m4, $T_{moho} = 600°C$, (c) m12, $T_{moho} = 550°C$, (d) m8, $T_{moho} = 500°C$. White lines denote the isotherms (200 °C increments). (e) shows the relationship between the times of slab break-off and continental T_{moho}. (f)-(h) are strain rate of models with various procontinental T_{moho}.

4.2 How crustal radioactive heat production influences the trajectory of the collision system

Radioactive elements are thought to mainly exist in the continental crust, and the radioactive heat production that originates from their decay is one of the important internal heat sources in the earth, which influences the continental lithospheric thermal structure significantly (Turcotte and Schubert, 2002; Faccenda et al., 2008). According to our model results, increasing the upper crustal H_r can distinctly increase the thermal gradient of the lithospheric upper part, under the effect of which the steep surface topography built at the early stage of continental collision would tend to be relatively gentle. In comparison, varying lower crustal H_r has much less influence on the variation of the lithospheric thermal gradient and the evolution of surface topography. Moreover, as the H_r in the crust increases, the lithospheric rheological strength decreases, which facilitates the growth of crustal shear zones. That is, the higher the crustal H_r, the more shear zones it may generate in the crust (Figs. 6c - 6i). In conclusion, crustal H_r is a crucial parameter in enhancing strain localization in the lithospheric

221 upper part that is closely related to the growth of shear zones, while it exerts a second-order influence on altering the

222 continental collision mode.
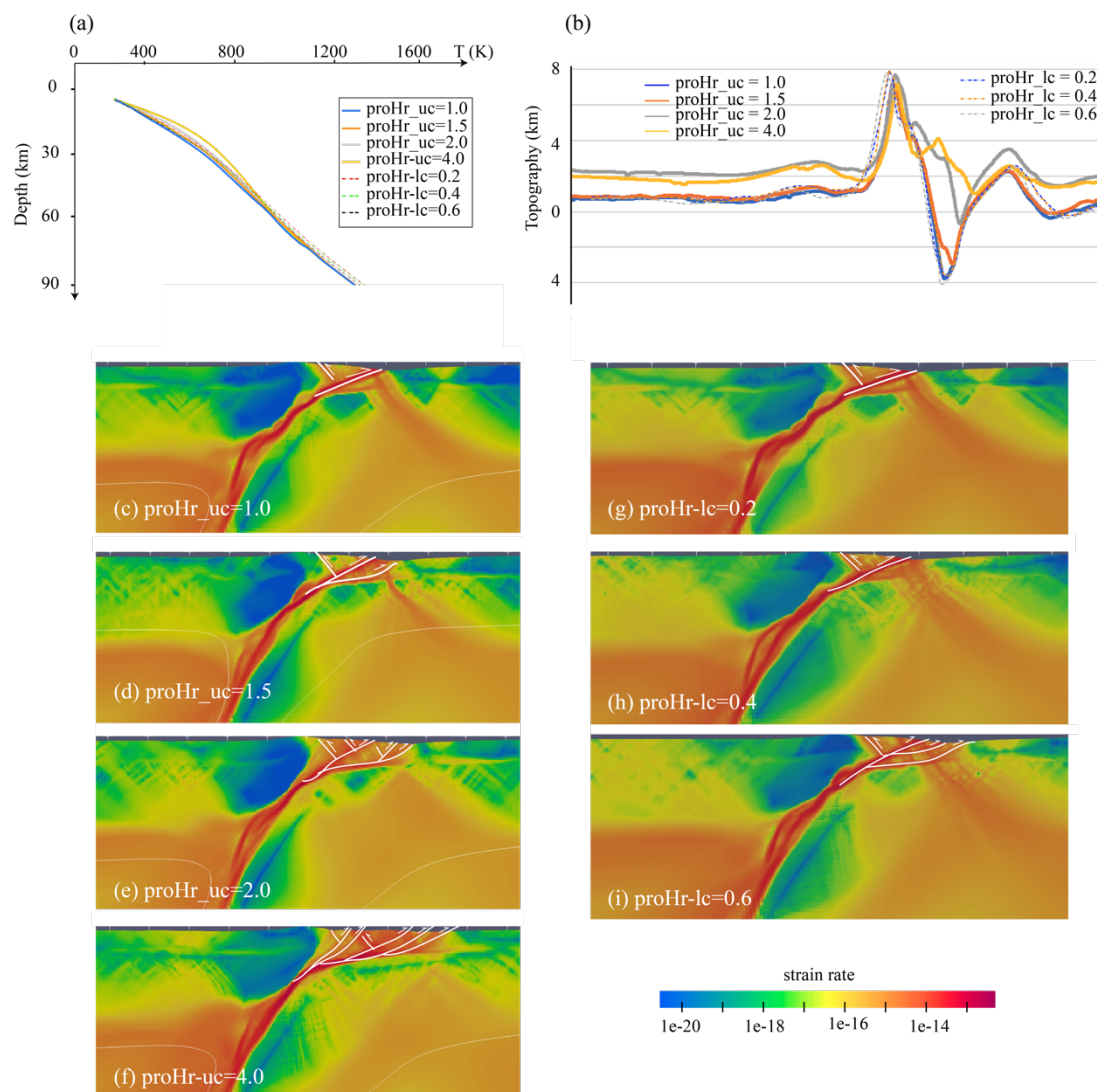
223

224 **Figure 6**. Temperature profiles (a), topography (b) and strain rate (c-i, at 20 Myr) of models with different crustal H_r.

225

4.3 Implications on the development of lateral heterogeneous of Indian-Asian collision

227   ~2000 km-long east-west Himalayan-Tibetan orogenic system was created by continental collision from ~ 60 to 50

228 Ma, with the Nanga Parbat syntaxis as its west margin and the Namche Barwa syntaxis in the east (Chen et al., 2015). It has

229 been proven by contrasting along-strike lithospheric structures (Li et al., 2008; Chen et al., 2015; Kufner et al., 2021). By

230   comparison, our models are capable of providing several first-order fits of the crust-mantle deformation behaviors to this

231   natural collision system, especially at the Hindu-Kush profile and the eastern Tibet profile.

232   Hindu Kush is the westernmost extend of the Himalayan-Tibetan orogen. Previous seismic tomography studies have

233   confirmed that there is a north-dipping, downward steepening, and thinning high-velocity anomaly (HVA), accompanied by

234   increasingly intense seismicity, underneath the region (Kufner et al., 2016; Kufner et al., 2021). The inclined HVA is

235   believed to be a subducting plate of Indian provenance and is part of the Indian-Asian collision system. The thinning of the

236   HVA is in the extent between 180-220 km, and was suggested to be at the transition zone between Indian continental

237   lithosphere and Neo-Tethys oceanic lithosphere. In agreement with the observations, Model m2 has a similar tectonic

238   background, and shows an analogous continuous subduction characterized by a nearly vertical dipping angle and a slab

239   necking at a depth of ~ 220 km. In addition, the relative narrow collision orogen in the model is also consistent with the

240   natural topography in this region (Figs. 7a, 2c). It's worth noticing that the observed inclined distribution of earthquakes

241   seems to coincide with the subducting continental crust. This may offer a possible explanation for the active intermediate

242   earthquakes beneath this region.

243   The main part of the Himalayan-Tibetan orogen is the product of a collision between the cold Indian craton and the

244   relative warm Asian continent after the closure of Neo-Tethys, the geological settings of which are quite analogous with our

245   Model m7. During the continental collision phase, the Yarlung Zangbo suture zone bordering the Indian and Asian

246   lithospheres moved significantly, creating an～8 km mountain (the Himalayas) and a ~ 4 km plateau (the Tibetan Plateau)

247   (Yin and Harrison, 2000). Unlike continuous subduction underlying the Hindu Kush, geological and seismological evidence

248   shows that the eastern part of the profile is underlain by a shallower-angle subducting Indian lithosphere following a slab

249   break-off; these are also similar to the model results of Model m7 (Figs. 7b, 2c). Furthermore, previous field observations

250   have shown that the northern part of the Indian continental crust is abundant with radioactive elements (Vidal et al., 1982;

251   Scaillet et al., 1990; Macfarlane, 1992; Faccenda et al., 2008). Our sensitive tests have recognized that continental crust with

252   high radioactive heat production is much easier to generate brittle fractures and intense deformation of the lithospheric upper

253   part, which may lead to the development of new shear zones (Fig. 6). This resembles the tectonic characteristics of large

254   thrust fault zones in the Himalayas (Fig. 7b).

255   In consequence, we speculate that the lithospheric thermal structural difference may be one of the key parameters that

256   control the evolution of lateral heterogeneity along the Himalayan-Tibetan orogen and that the high content of crustal

257   radioactive elements is one of the significant factors that dominates the growth of large thrust fault zones in the Himalayas.
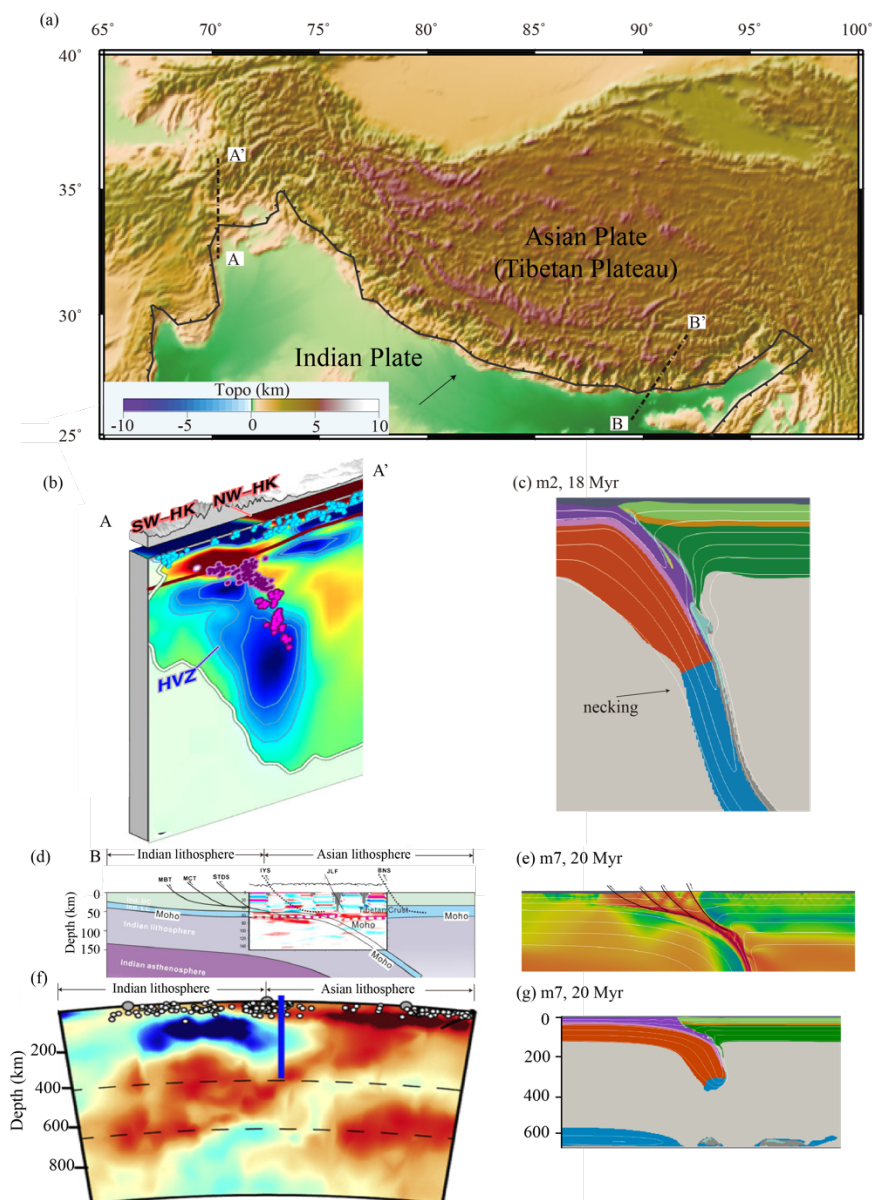
Figure 7. (a) Geographic setting of Himalayan-Tibetan orogen. Schematic geologic cross-sections across the (b) western (Hindu Kush) (Kufner et al., 2021) and eastern Himalayan-Tibetan orogen (Li et al., 2008; Wang et al., 2019). (c) shows the compositional field of Model m2 (mode I), (e) and (g) are the strain rate and compositional field of Model m7 (mode II), respectively.

5 Conclusions

In this work, we systematically discuss the influences of the lithospheric thermal structure on the evolution of the continental collision system based on high-resolution thermomechanical numerical experiments. The model results demonstrate that:

Two end members of continental collision are obtained: the continuous subduction mainly occurs with a relative cold overriding lithosphere ($T_{moho} \leq 450°$), and as the retrocontinental T_{moho} increases, the subducting angle steepens. Slab break-off dominates when the model has a relative hot procontinental T_{moho} (≥ 500 °C), especially when the retrocontinental T_{moho} is greater than $550°C$. H_r is a second-order controlling parameter compared with T_{moho} in shaping the continental collision mode, while it is more prone to facilitate the growth of crustal shear zones.

The lithospheric thermal structure may have played a significant role in the development of lateral heterogeneity along the Himalayan-Tibetan orogenic belt. We suggest that the different evolutionary paths between the continuous subduction underlying the Hindu Kush and the continental subduction beneath eastern Tibet may come from the inherited lateral inhomogeneous of the Indian lithospheric geothermal gradient. In addition, the high content of radioactive elements in the continental crust may be one of the important reasons for the development of deep and large thrust fault zones in this collision orogen.

Data availability. The input files of ASPECT are available at the Open Science Framework repository with https://doi.org/10.5281/zenodo.8076545.

Competing interests. The authors declare that they have no conflict of interest.

Author contributions. MXL and DHY designed and oversaw the project. MXL performed all the numerical simulations. R.Q. participated in the discussions and paper revisions. All authors contributed to the manuscript writing.

Acknowledgment. This work is supported by the National Natural Science Foundation of China (Grant Nos. 42104097, U1839206). The figures in this paper are produced by the Paraview V5.11.1, Generic Mapping Tools V5.4.2 (Wessel et al., 2013), Python V3.6.7, and Adobe Illustrator. We thank the Computational Infrastructure for Geodynamics for supporting the development of ASPECT (https://aspect.geodynamics.org). ASPECT (version 2.4.0-pre) we used in this paper is built on the open-source finite element package deal. II (version 10.0.0-pre) through the candi installation package (https://github.com/dealii/candi). Additional dependencies include Trilinos (13.0.0) and p4est (2.2.0). All the numerical models were run on the TianHe-1A cluster at National Supercomputer Center in Tianjin.

References

Arndt, D., Bangerth, W., Blais, B., Fehling, M., Gassmöller, R., Heister, T., Heltai, L., Köcher, U., Kronbichler, M., Maier, M., Munch, P., Pelteret, J.-P., Proell, S., Simon, K., Turcksin, B., Wells, D., and Zhang, J.: The deal.II library, Version 9.3. J. Numer. Math., 29 (3), 171-186, https://doi.org/10.1515/jnma-2021-0081, 2021.

Beaumont, C., Fullsack, P., and Hamilton, J.: Styles of crustal deformation in compressional orogens caused by subduction of the underlying lithosphere. Tectonophysics, 232, 119-132, https://doi.org/10.1016/0040-1951(94)90079-5, 1994.

Chapman, D.S.: Thermal gradients in the continental crust. Geological Society, London, Special Publications 24, 63-70, https://doi.org/10.1144/GSL.SP.1986.024.01.0, 1986.

Chen, L., and T. V. Gerya.: The role of lateral lithospheric strength heterogeneities in orogenic plateau growth: Insights from 3-D thermo-mechanical modeling, J. geophys. Res.: Solid Earth, 121(4), 3118-3138, https://doi.org/10.1002/2016JB012872, 2016.

Chen, Y., L, W., Yuan, X. H., Badal, J., and Teng, J. W.: Tearing of the Indian lithospheric slab beneath southern Tibet revealed by SKS-wave splitting measurements. Earth Planet. Sci. Lett., 413: 13-24, https://doi.org/10.1016/j.epsl.2014.12.041, 2015.

Davis, R.O., and Selvadurai, A.P.S.: Plasticity and Geomechanics. Cambridge University Press, Cambridge, 2002.

Faccenda, M., Gerya, T.V., and Chakraborty, S.: Styles of post-subduction collisional orogeny: Influence of convergence velocity, crustal rheology and radiogenic heat production. Lithos, 103, 257-287, https://doi.org/10.1016/j.lithos.2007.09.009, 2008.

Ghazian, R.K., and Buiter, S.J.H.: A numerical investigation of continental collision styles. Geophys. J. Int., 193, 1133-1152, https://doi.org/10.1093/gji/ggt068, 2013.

Gleason, G.C., and Tullis, J.: A flow law for dislocation creep of quartz aggregates determined with the molten salt cell. Tectonophysics 247, 1-23, https://doi.org/10.1016/0040-1951(95)00011-B, 1995.

Glerum, A., Thieulot, C., Fraters, M., Blom, C., and Spakman, W.: Nonlinear viscoplasticity in ASPECT: benchmarking and applications to subduction. Solid Earth, 9, 267-294, https://doi.org/10.5194/se-9-267-2018, 2018.

Heron, P.J., and Pysklywec, R.N.: Inherited structure and coupled crust-mantle lithosphere evolution: Numerical models of Central Australia. Geophys. Res. Lett., 43, 4962-4970, https://doi.org/10.1002/2016GL068562, 2016.

Hirth, G., and Kohlstedt, D.: Rheology of the upper mantle and the mantle wedge: A view from the experimentalists. Washington DC American Geophysical Union Geophysical Monograph Series, 138, 83-105, https://doi.org/10.1029/138GM06, 2003.

Huangfu, P., Li, Z.H., Fan, W., and Shi, Y.: Dynamics of crustal overthrust versus underthrust in the continental collision zones: Numerical modelling. Terra Nova, 31, 332-342, https://doi.org/10.1111/ter.12384, 2019.

Huangfu, P., Wang, Y., Fan, W., Li, Z., and Zhou, Y.: Dynamics of unstable continental subduction: Insights from numerical modeling. Sci. China. Earth. Sci., 60, 218-234, https://doi.org/10.1007/s11430-016-5014-6, 2017.

328 Karato, S.-i., and Wu, P.: Rheology of the upper mantle: A synthesis. Science, 260, 771-778,
329   https://doi.org/10.1126/science.260.5109.771, 1993.

330 Karato, S.-i.: Deformation of Earth Materials: An Introduction to the Rheology of Solid Earth. Cambridge University Press,
331   Cambridge, 2008.

332 Kronbichler, M., Heister, T., and Bangerth, W.: High accuracy mantle convection simulation through modern numerical
333   methods. Geophys. J. Int., 191, 12-29, https://doi.org/10.1111/j.1365-246X.2012.05609.x, 2012.

334 Kufner, S. K., Kakar, N., Bezada, M., Bloch, W., and Schurr, B.: The Hindu Kush slab break-off as revealed by deep
335   structure and crustal deformation. Nature Communications, 12: 1685, https://doi.org/10.1038/s41467-021-21760-w,
336   2021.

337 Kufner S. K., Schurr, B., Sippl, C., Yuan, X. H., Ratschbacher, L., Akbar, A. M., Ischuk, A., Murodkulov, S., Schneider, F.,
338   Mechie, J., and Tilmann, F.: Deep india meets deep asia: lithospheric indentation, delamination and break-off under
339   pamir and hindu kush (central asia). Earth Planet. Sci. Lett., 435, 171-184, https://doi.org/10.1016/j.epsl.2015.11.046,
340   2016.

341 Li, C., van der Hilst, R. D., Meltzer, A. S., and Engdahl, E. R.: Subduction of the Indian lithosphere beneath the Tibetan
342   Plateau and Burma. Earth Planet. Sci. Lett. 274, 157–168, https://doi.org/10.1016/j.epsl.2008.07.016, 2008.

343 Liao, J., and Gerya, T.: Partitioning of crustal shortening during continental collision: 2-D thermomechanical modeling. J.
344   geophys. Res., 122, 592-606, https://doi.org/10.1002/2016JB013398, 2017.

345 Liu, M., and Yang, D. H.: How do pre-existing weak zones and rheological layering of the continental lithosphere influence
346   the development and evolution of intra-continental subduction? J. Asian. Earth. Sci., 238, 105385,
347   https://doi.org/10.1016/j.jseaes.2022.105385, 2022.

348 Liu, M., Yang, D. H., and Huangfu, P. P.: Effects of plate velocity slowdown on altering continental collision patterns and
349   crustal-lithospheric deformation during the collision process. Front. Earth Sci., 10: 814710,
350   https://doi.org/10.3389/feart.2022.814710, 2022a.

351 Liu, S., Sobolev, S.V., Babeyko, A.Y., and Pons, M.: Controls of the foreland feformation pattern in the orogen-foreland
352   shortening system: constraints from high-resolution geodynamic models. Tectonics, 41, e2021TC007121,
353   https://doi.org/10.1029/2021TC007121, 2022b.

354 Luth, S., Willingshofer, E., Sokoutis, D., and Cloetingh, S.: Analogue modelling of continental collision: Influence of plate
355   coupling on mantle lithosphere subduction, crustal deformation and surface topography. Tectonophysics, 484, 87-102,
356   https://doi.org/10.1016/j.tecto.2009.08.043, 2010.

357 Macfarlane, A.M.: The tectonic evolution of the core of the Himalaya, Langtang National Park, central Nepal. Massachusetts
358   Institute of Technology, 1992.

359 Pysklywec, R.N.: Evolution of subducting mantle lithosphere at a continental plate boundary. Geophys. Res. Lett., 28, 4399-
360   4402, https://doi.org/10.1029/2001GL013567, 2001.

361 Rybacki, E., Gottschalk, M., Wirth, R., and Dresen, G.: Influence of water fugacity and activation volume on the flow
362   properties of fine-grained anorthite aggregates. J. geophys. Res., 111, B03203, https://doi.org/10.1029/2005JB003663,
363   2006.

364 Scaillet, B., France-Lanord, C., and Le Fort, P.: Badrinath-Gangotri plutons (Garhwal, India): petrological and geochemical
365   evidence for fractionation processes in a high Himalayan leucogranite. J. Volcanol. Geoth. Res., 44, 163-188,
366   https://doi.org/10.1016/0377-0273(90)90017-A, 1990.

367 Tang, J., Chen, L., Meng, Q., and Wu, G.: The effects of the thermal state of overriding continental plate on subduction
368   dynamics: Two-dimensional thermal-mechanical modeling. Sci. China. Earth., Sci, 63, 1519-1539,
369   https://doi.org/10.1007/s11430-019-9624-1, 2020.

370 Toussaint, G., Burov, E., and Jolivet, L.: Continental plate collision: Unstable vs. stable slab dynamics. Geology, 32, 33-36,
371   https://doi.org/10.1130/G19883.1, 2004.

372 Turcotte, D.L., and Schubert, G.: Geodynamics. Cambridge university press. 2002

373 Ueda, K., Gerya, T.V., and Burg, J.-P.: Delamination in collisional orogens: Thermomechanical modeling. J. geophys. Res.,
374   117, B08202, https://doi.org/10.1029/2012JB009144, 2012.

375 van Zelst, I., F. Crameri, A. E. Pusok, A. Glerum, J. Dannberg, and C. Thieulot.: 101 geodynamic modelling: how to design,
376   interpret, and communicate numerical studies of the solid Earth, Solid Earth, 13(3), 583-637, https://doi.org/10.5194/se-
377   13-583-2022, 2022.

378 Vidal, P., Cocherie, A., and Fort, P.L.: Geochemical investigations of the origin of the Manaslu leucogranite (Himalaya,
379   Nepal). Geochim. Cosmochim. Ac., 46, 2279-2292, https://doi.org/10.1016/0016-7037(82)90201-0, 1982.

380 Vogt, K., Willingshofer, E., Matenco, L., Sokoutis, D., Gerya, T., and Cloetingh, S.: The role of lateral strength contrasts in
381   orogenesis: A 2D numerical study. Tectonophysics, 746, 549-561, https://doi.org/10.1016/j.tecto.2017.08.010, 2018.

382 Wang, C. Y., Mooney, W. D., Zhu, L., Wang, X., Lou, H., and You, H., Cao, Z., Chang, L., and Yao, Z.: Deep structure of
383   the eastern himalayan collision zone: evidence for underthrusting and delamination in the postcollisional stage.
384   Tectonics, 38,3614-3628, https://doi.org/10.1029/2019TC005483, 2019.

385 Wessel, P., Smith, W.H.F., Scharroo, R., Luis, J., and Wobbe, F.: Generic Mapping Tools: Improved Version Released. Eos,
386   Transactions American Geophysical Union, 94, 409-410, https://doi.org/10.1002/2013EO450001, 2013.

387 Wilks, K.R., and Carter, N.L.: Rheology of some continental lower crustal rocks. Tectonophysics, 182, 57-77,
388   https://doi.org/10.1016/0040-1951(90)90342-6, 1990.

389 Willingshofer, E., and Sokoutis, D.: Decoupling along plate boundaries: Key variable controlling the mode of deformation
390   and the geometry of collisional mountain belts. Geology, 37, 39-42, https://doi.org/10.1130/G25321A.1, 2009.

391 Yin, A., and Harrison, T.M.: Geologic Evolution of the Himalayan–Tibetan Orogen. Annu. Rev. Earth. Pl. Sc., 28, 211-280,
392   2000

393 Zhou, H. W., and Murphy, M. A.: Tomographic evidence for wholesale underthrusting of india beneath the entire tibetan
394   plateau. J. Asian. Earth. Sci., 25(3), 445-457, https://doi.org/10.1016/j.jseaes.2004.04.007, 2005.